ACS Catalysis

Research Article

pubs.acs.org/acscatalysis

High-Performance, Ultralow Platinum Membrane Electrode Assembly Fabricated by In Situ Deposition of a Pt Shell Layer on Carbon-Supported Pd Nanoparticles in the Catalyst Layer Using a Facile Pulse Electrodeposition Approach

Dai Dang, Haobin Zou, Zi'ang Xiong, Sanying Hou, Ting Shu, Haoxiong Nan, Xiaoyuan Zeng, Jianhuang Zeng, and Shijun Liao*

School of Chemistry and Chemical Engineering, South China University of Technology, The Key Laboratory of Fuel Cell Technology of Guangdong Province & The Key Laboratory of New Energy Technology of Guangdong Universities, Guangzhou 510641, China

ABSTRACT: An ultralow platinum loading membrane electrode assembly (MEA) is prepared by a facile synthesis process in which pulse electrodeposition is used to achieve a catalyst layer by the in situ decoration of carbon-supported Pd nanoparticles with a thin layer of Pt atoms. The novel MEA exhibits excellent performance in a H_2/air single fuel cell, with Pt loading of as little as 0.015 mg cm^{-2} at the anode and 0.04 mg cm^{-2} at the cathode, outperforming the commercial Pt/C MEA (Johnson Matthey, 40 wt % Pt). The shift in binding energy of the XPS peak of Pd and Pt in the Pd@Pt/C MEA confirms the presence of the Pt shell and the interaction between the shell and the Pd core. We suggest that the high performance of this Pd@Pt/C MEA may be due to several factors: high Pt dispersion arising from the core−shell structure, high Pt utilization because there is no Nafion binder covering the Pt, the quantum effect caused by the high distribution of Pt, and the interaction between the Pt shell and the Pd in the core.

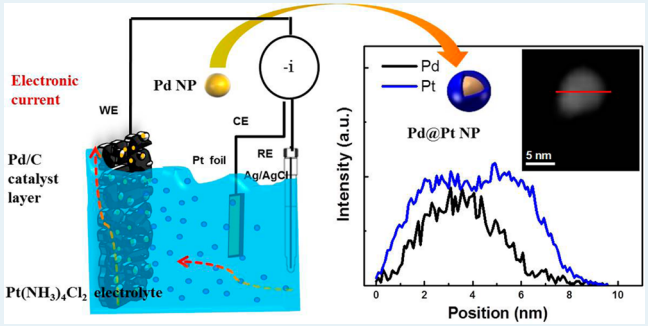

KEYWORDS: *ultralow platinum, core−shell structure, pulse electrodeposition, membrane electrode assembly, fuel cell*

1. INTRODUCTION

The use of fossil fuels has long been identified as a key factor in global environmental deterioration. Consequently, researchers around the world have been keen to find alternative energy sources or to develop energy conversion devices that are more efficient than the internal combustion engine. For the past few decades, proton exchange membrane fuel cells (PEMFCs) have been favored for their zero emissions and high efficiency.[1−3] Unfortunately, the high cost, caused mainly by the usage of platinum at a relatively larger amount, is becoming a major obstacle to hinder its commercialization.[3,4] It is therefore very important to substantially reduce the amount of platinum in a fuel cell.[5] The most common and desired approach to achieve this target is to design ultrafine core−shell structured nanoparticles by coating active Pt atoms on the surface of a core material (Pd, Ru, Ir, Co, etc.)[6−16] that has tunable activity and an enlarged Pt electrochemical specific surface area.[7,17−19] However, it has been recognized that the enhanced utilization of such Pt-based electrocatalysts in PEMFCs not only depends on the nature of catalytic activity but also relies on the inner structure of the catalyst layer that is sandwiched between the gas diffusion layer and solid polymer electrolyte to form the essential part of the MEA.[3]

Conventionally, carbon supported core−shell nanoparticles are mixed with binding materials such as polytetrafluoroethylene or Nafion ionomer either by a catalyst-coated membrane (CCM) process, or sprayed onto the gas diffusion layer, followed by hot-pressing to making membrane electrode assemblies (MEAs).[7,20] Not all of the catalyst's Pt surface area theoretically available for electrochemical reaction can be exposed, leading to relatively low Pt utilization. This can be explained in two ways: (i) active Pt NPs embedded in the carbon powder may lose contact with or have insufficient contact with the solid electrolyte; (ii) Pt catalyst particles may become electrically isolated or encapsulated in the interior area by a film of the electrically nonconducting solid electrolyte.[3,21] These issues make it difficult to establish good contact between the catalyst and the reactant to form an electron-conducting path or proton-conducting path, respectively. On the other hand, the intrinsic Pt surface area of a catalyst performing on a glassy carbon disk electrode is larger than the Pt surface area measured by cyclic voltammetry in an MEA, and the ratio of the S_{PtMEA} to S_{Ptcata} varies, depending on the MEA preparation

Received: January 8, 2015
Revised: June 7, 2015
Published: June 8, 2015

DOI: 10.1021/acscatal.5b00030
ACS Catal. 2015, 5, 4318−4324

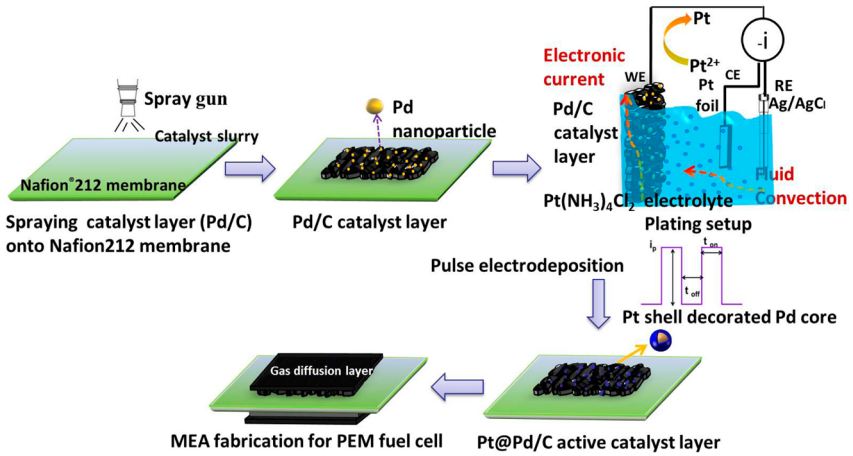

Figure 1. Schematic diagram of in situ construction of the Pd@Pt/C catalyst on the electrode and fabrication procedure for the MEA.

method.[3,22,23] Therefore, it is usually suggested that high Pt loading is required for a classical MEA (cathode: 0.4 mg cm^{-2}, anode: 0.2 mg cm^{-2}) to compensate for the unsatisfactory Pt utilization. In this regard, more attention should be paid to MEA engineering to develop a well-refined core−shell structured NP within the catalyst layer to improve Pt utilization efficiency as well as maintain high performance and good stability.

Herein, we describe an environmentally friendly ("green") and facile synthetic strategy for the in situ construction of a catalyst layer directly on the surface of an electrode, using a pulse electrodeposition (PED) approach, through which the synthesis of core−shell structured catalysts and making the MEA can be simplified. In this work, the PED method plays an essential role in achieving Pt deposition and allows one to tune the amount of Pt while using a green process with handy procedures and timesaving operations. This technology anchors the Pt atoms on the Pd surface while maximizing the exposure of the core−shell electrocatalysts to the three-phase boundary and substantially enhancing Pt utilization in the electrochemical reactions. The Pd@Pt/C MEA prepared by the present method has an ultralow Pt loading of 0.04 mg cm^{-2} at the cathode and outperforms the commercial Johnson Matthey Pt/C MEA (JM, 40% Pt) with a Pt loading of 0.1 mg cm^{-2}. This novel Pd@Pt/C MEA takes advantage of its unique characteristics, resulting in a promising candidate for the next generation of state-of-the-art MEAs.

2. EXPERIMENTAL SECTION

2.1. Preparation of Pd@Pt/C MEA. The fabrication procedure for the Pd@Pt/C MEA is described in Figure 1. Only two steps were employed to synthesize the Pd@Pt/C electrode: (i) preparation of Pd/C base catalyst layer(s) on one or both sides of the Nafion212 membrane by a CCM approach[24] and (ii) PED of the Pt layer(s) (several atoms thick) on the surface of Pd NPs embedded in the Pd/C catalyst layer. Using this strategy, the Pt atoms were deposited only on the exposed surfaces of Pd NPs dispersed on the outer and interior surfaces of the Pd/C catalyst layer, and since no Pt atoms were covered by Nafion binder, theoretically, the Pt utilization could be substantially enhanced.

In the first step, Pd/C catalysts were synthesized by an organic colloidal method reported elsewhere,[25] then the as-prepared Pd/C (20 wt % Pd) catalysts were mixed with 5 wt % Nafion ionomer solution (DuPont, USA) and isopropyl alcohol, and this mixture was sprayed onto one side of the membrane. The weight ratio of the Pd/C catalyst to dry Nafion was 2.5:1. In the second step, galvanostatic PED was carried out in a three-electrode cell using a homemade setup whereby the Pd@Pt/C MEA was fabricated. Brifely, the Pd/C-based MEA was framed within a fixed and exposed area of 5 cm^2, with the Pd/C base layer serving as the working electrode and platinum wire and an Ag/AgCl electrode (3 M KCl) as the counter and reference electrodes, respectively. Peak current densities were set to 50 mA cm^{-2} with 0.3 ms of the time on and 0.15 ms of time off for the PED process. After the PED process, the MEAs were emerged in 0.5 M H_2SO_4 solution at 70 °C for 30 min to remove the possible Cl^- contaminant. The Pt loading of the Pd@Pt/C MEA was detected by atomic absorption spectroscopy (AAS). For comparison, the JM Pt/C MEA was prepared via the method previously reported by our group[24] using JM Pt/C (Johnson Matthey, 40% Pt) catalyst for both anode and cathode.

2.2. Fuel Cell Measurements. The MEA was assembled by putting gas diffusion layers—prepared by spraying a carbon−Teflon mixture onto pretreated carbon paper—on the anode and cathode sides. MEA performance was evaluated using a Fuel Cell Testing System (Arbin Instruments, USA). The cell temperature was set to be 70 °C with a back pressure of 30 psi for both the anode and cathode. Pure hydrogen and air were externally humidified (100% humidification) before being fed at a gas flow rate of 120 sccm min^{-1} for hydrogen and 800 sccm min^{-1} for air.

2.3. Characterizations of the MEAs. The morphologies of the Pd@Pt/C catalysts were characterized by transmission electron microscopy and energy dispersive X-ray spectroscopy (EDS) line scan using a TECNAI G2 F30 transmission electron microscope (FEI Inc., Valley City, ND) at 300 kV. X-ray diffraction (TD-3500, Tongda, China) was employed to investigate the crystal structure of the catalysts. The element binding energies were analyzed by X-ray photoelectron spectroscopy (XPS) on a PerkinElmer PHI1600 system (PerkinElmer, USA) using a single Mg Kα X-ray source operating at 300 W and 15 kV.

2.4. Electrochemical Measurements of the MEAs. Electrochemical impedance spectroscopy and cyclic voltammetry (CV) were performed on a Zahner IM6e electrochemistry station (Zahner, Germany). The measurements were carried out at a cell potential of 0.8 V with an amplitude of 5 mV and in the frequency range of 0.1−1000 Hz. CV measurements were

DOI: 10.1021/acscatal.5b00030
ACS Catal. 2015, 5, 4318−4324

conducted at room temperature, 25 °C, using humidified N_2 at the cathode (working electrode) and humidified H_2 at the anode.

3. RESULTS AND DISCUSSION

The structure and morphology of the Pd/C and Pd@Pt/C catalysts, which were washed off from the MEA surface with ethanol, were investigated by TEM. As shown in Figure 2a, all

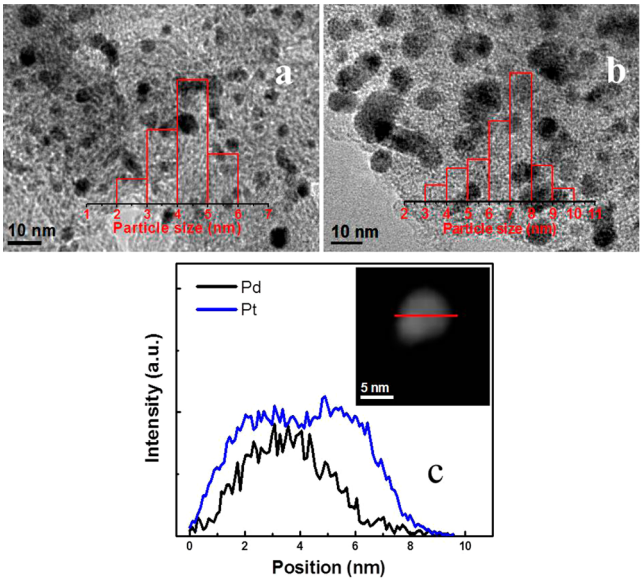

Figure 2. TEM images and corresponding particle size distribution histograms (inset) of (a) Pd/C and (b) Pd@Pt/C; and STEM image of a single particle of Pd@Pt/C (inset), along with the corresponding EDS line-scanning profile (c).

the Pd NPs had an average grain size of ~4.5 nm and were highly distributed on the carbon support. Conversely, most of the Pd@Pt nanoparticles obtained by PED were 6−8 nm in diameter (Figure 2b), with a mean particle size of ~7.5 nm. The thickness of the Pt layer was ~1−2 nm, corresponding to 3−6 atomic layers. The slight increase in particle size may be ascribed to the reduced Pt atoms that were uniformly deposited on the Pd NPs to form a core−shell structure. This core−shell structure and element distribution were further confirmed using scanning transmission electron microscopy/EDS line scan analysis. A single nanoparticle of Pd@Pt catalyst was chosen for line scanning (Figure 2c). The higher Pt intensity at the edge clearly demonstrates the formation of the core−shell structure. We suggest that the Pt ions selectively settled on the surface of the Pd particle for two reasons: (i) intimate surface energy between Pd and Pt (in this situation, Pt preferentially deposited on the Pd because the interface tension between Pt and Pd is much less than that between Pt and carbon);[26] and (ii) Pd NPs can be more electronic conducted than XC-72R carbon powder, so on the Pd surface, Pt^{2+} ions would easily capture the electrons to get reduced.

X-ray diffraction patterns were obtained to reveal the structural changes between the Pd/C catalyst layer in the Pd/C MEA and the Pd@Pt/C catalyst layer in the Pd@Pt/C MEA. As shown in Figure 3, the peaks situated at ~16.9° are typical features of the Nafion membrane, their intensity so strong that the graphitic nature of the nearby carbon support appears to have been weakened. The Pd/C MEA, which was used as the

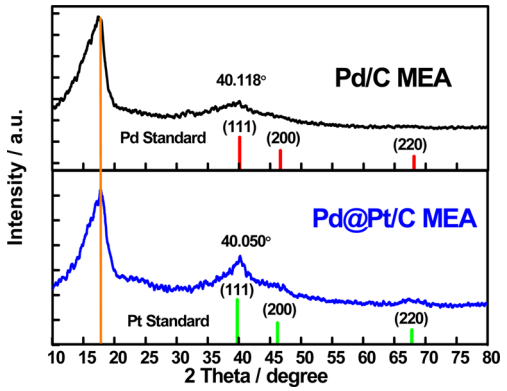

Figure 3. XRD patterns of Pd/C MEA, Pd standard (shown as red vertical lines), Pd@Pt/C MEA, and Pt standard (shown as green vertical lines).

base material for a further PED process, exhibited very weak XRD patterns compared with Pd standard (shown by the red vertical lines). This phenomenon may be explained by the possible binding effects of Nafion (undetectable with X-rays). In contrast, the (111) peak and (220) peak at Bragg angles of around 40° and 68° gradually became distinct after PED of the Pt, signaling the surface deposition of platinum. Although the Pt loading was as low as 0.04 mg cm^{-2} (compared with the Pd loading of 0.05 mg cm^{-2}), every Pt atom was exposed to X-ray radiation rather than being hidden beneath the Nafion ionomer. Furthermore, the refined Pt lattice parameters for the Pt shell of the Pd@Pt MEA presented a 3.8934 Å f.c.c. lattice constant, which was slightly compressed compared with the Pt/C MEA (3.923 Å) reported in our previous research.[8] In addition, the (111) diffraction peak position of the Pd@Pt/C MEA was slightly shifted to a higher 2θ angle compared with the standard Pt XRD pattern shown by the green vertical lines. It is important that no obvious strong diffraction peaks of Pt could be observed in the XRD patterns, indicating that the Pt atoms were deposited on the surface of the Pd NPs to form a thin shell layer.

To further confirm the existence of Pt shell layer decorating the surface of Pd nanoparticles and probe into the synergic effect generated by surface electronic tuning, we obtained the XPS spectra of Pd@Pt/C, Pt/C, and Pd/C for the Pt 4f and Pd 3d regions. As shown in Figure 4a,b, the Pt 4f peak in these two samples can be deconvoluted into two pairs of doublets. The Pt 4f7/2 signal of Pd@Pt/C shifted to a higher binding energy (71.53 eV) compared with the Pt 4f7/2 signal of Pt/C (71.32 eV).

On the other hand, the Pd in the core shows a very distinctive set of XPS spectra. Figure 4c,d shows that the Pd 3d5/2 signal of Pd@Pt/C shifted to a higher binding energy (335.45 eV) relative to the Pd 3d5/2 peak of Pd/C (335.09 eV). This positive shift (~0.36 eV) in the Pd binding energy indicates a strong electronic interaction between the Pd in the core and the Pt on its surface. This result is consistent with those reported by others previously.[27,28] The observed changes in binding energy of core−shell catalysts could be attributed to the electronic coupling between the Pt shell and Pd substrate.[29] Meanwhile, a compressive lattice strain induced by placing the Pt shell with a lager lattice parameter (3.9232 Å) on a Pd substrate with a smaller lattice parameter (3.8898 Å) would be another factor causing the positive shift of Pt 4f signals in our core−shell particles.[30−32] Furthermore, as shown in Figure 4a,b,

DOI: 10.1021/acscatal.5b00030
ACS Catal. 2015, 5, 4318−4324

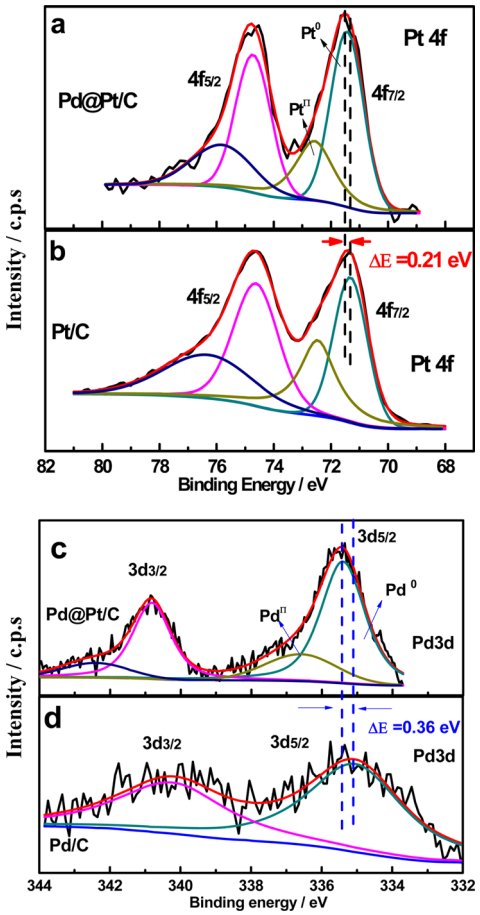

Figure 4. XPS spectra of (a) Pt 4f in Pd@Pt/C, (b) Pt 4f in Pt/C, (c) Pd 3d in Pd@Pt/C, and (d) Pd 3d in Pd/C.

clearly, the Pd@Pt/C catalyst exhibits higher Pt^0 proportion (66.6%) than that in commercial Pt/C catalyst (54.5%). The relatively low content of oxide state of Pt in Pd@Pt/C catalysts suggests a weaker oxophilicity than commercial Pt/C catalyst.

It should be mentioned that the electronic tuning occurred between the different metal components has been intensively discussed by other groups.[33−35] It is well-understood that the electronic structure of Pt decorated on the Pd/C surface is different from that of bulk Pt as a result of the so-called strain and ligand effects of the core materials. The electronic tuning between the metal in the shell layer and the core metal(s) may be attributed to the difference of their electronegativities called ligand effect, as well as the strain effect induced by the lattice mismatching of shell layer and core material.

For our catalyst system, the larger electronegativity of Pt (2.28) than Pd (2.20) may cause the ligand effect; in addition, the strain effect, caused by the lattice difference of Pt and Pd (3.923 and 3.890 Å) may make a significant contribution to the surface electronic tuning.

Figure 5 shows the cyclic voltammograms (CV) plots obtained in a single fuel cell environment. It can be observed that the H_2 desorption peaks of the Pd@Pt/C MEA in the range of 0.1−0.3 V increased after the Pt deposition on the surface of the Pd/C MEA. Because CV plots play a vital role in probing the surface structure, the peak intensity increase in the hydrogen desorption region of the Pd@Pt/C MEA would serve as further indirect evidence for the formation of a core−shell structure. Because of the high dispersion of platinum on the Pd

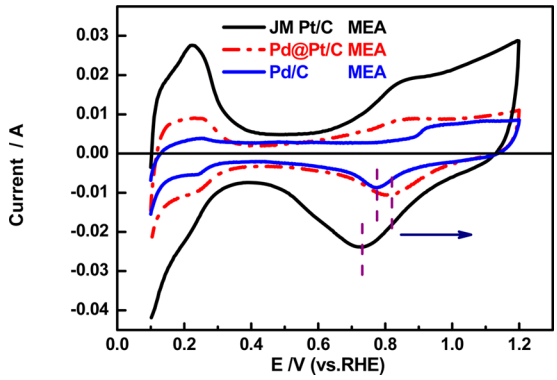

Figure 5. Cyclic voltammograms of JM Pt/C MEA 0.1 mg_{Pt} cm^{-2}, Pd@Pt/C MEA 0.04 mg_{Pt} cm^{-2} and Pd/C MEA. The measurements were performed at 27 °C using humidified N_2 at the cathode (working electrode) and humidified H_2 at the anode (counter electrode and reference electrode). Scan rate: 0.05 V s^{-1}.

core, the calculated ECSA of the Pd@Pt/C MEA can still reach 61.9 m^2 g^{-1}_{Pt}, which is 70% ECSA of JM Pt/C MEA (86.1 m^2 g^{-1}_{Pt}). However, the Pt loading of the Pd@Pt/C MEA is just 40% of that for JM Pt/C MEA, which might indicate the former's higher Pt utilization efficiency. Intriguingly, compared with JM Pt/C MEA, a positive shift of oxide (OH_{ads}) adsorption and desorption peak in the Pd@Pt/C MEA in the region of 0.7−0.9 V was discovered. This implies a weaker binding of OH species on the surface of the Pd@Pd, as illustrated by XPS analysis, and thus may improve the catalytic activity and durability of the catalysts.[3,36,37]

The catalytic activity of the Pd@Pt/C MEA as the anode in a single PEM fuel cell was investigated using H_2 and air as the fuel and oxidant gases at 70 °C. As shown in Figure 6a, when we compare the performance of the MEA prepared using a JM Pt/C catalyst that has 4.3 times the Pt loading at the anode, we observe that the Pd@Pt/C MEA has better performance across the whole polarization region. Even taking into account the total amount of metal (Pd + Pt), the performance of the Pd@Pt/C MEA still surpasses that of the JM Pt/C MEA. The mass-specific activity was benchmarked against the Pt and total metal loadings, as shown in Figure 6b, demonstrating that the Pd@Pt/C MEA was almost 5.4 times and 1.2 times higher than the JM Pt/C MEA, respectively. The maximum power density was as high as 780 mW cm^{-2} for the Pd@Pt/C MEA, compared with 610 mW cm^{-2} for the commercial JM Pt/C electrode. The enhancement in H_2/air cell performance demonstrates the MEA's superior Pt utilization and mass-transport profile. This remarkable electrocatalytic activity is specifically attributable to the in situ construction of the core−shell nanoparticles at the three-phase boundary on the MEA, which results in surface electronic tuning between the Pd and Pt d-band centers and substantially reduces the amount of Pt used.

Figure 7a presents the typical single-cell performances for both Pd@Pt/C MEA (0.04 mg_{Pt} cm^{-2}) and JM Pt/C MEA (0.1 mg_{Pt} cm^{-2}) as cathode catalysts under the following operating conditions: 70 °C for cell, H_2, and air temperature; 5 cm^2 effective area; 30 psi back pressure. The JM Pt/C (0.1 mg_{Pt} cm^{-2}) was prepared as the anode for these two MEAs. The MEA with Pd@Pt/C catalyst exhibited a much better performance than the JM Pt/C MEA across the entire electrochemical reaction region. It is important and interesting that even when the platinum loading was as low as 0.04 mg cm^{-2} at the cathode, the Pd@Pt/C MEA still maintained an

DOI: 10.1021/acscatal.5b00030
ACS Catal. 2015, 5, 4318−4324

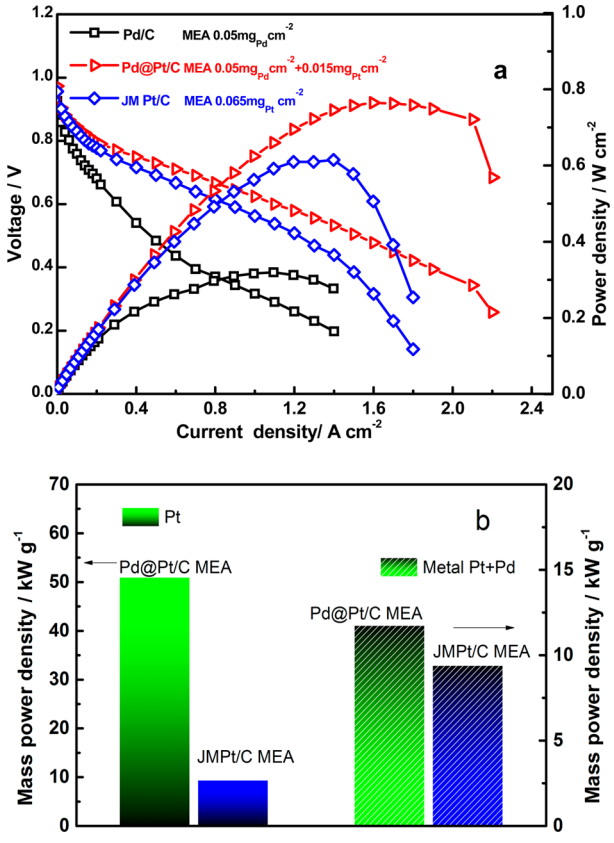

Figure 6. (a) Polarization curves for single-cell performance and (b) mass activity comparison for the MEAs with different anode compositions and identical cathodes (JM Pt/C 0.2 mg$_{Pt}$ cm^{-2}).

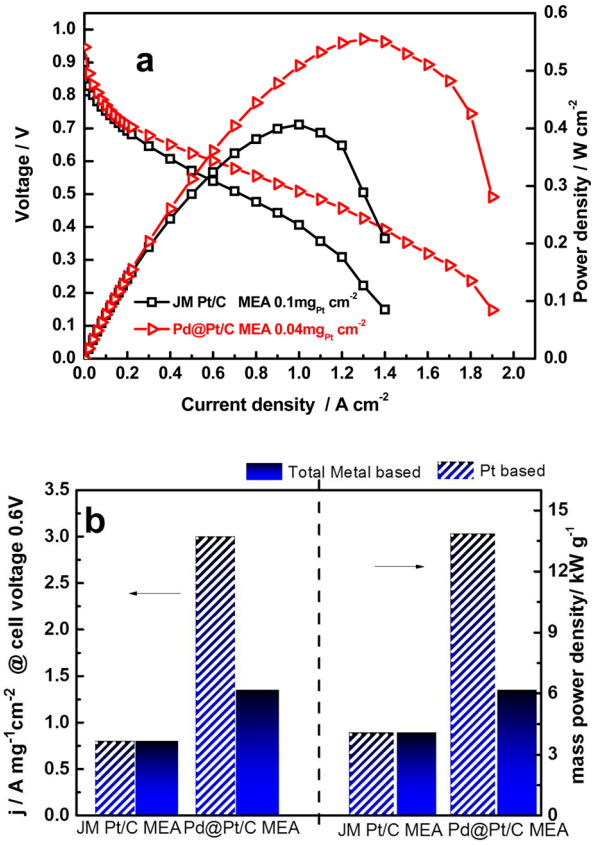

Figure 7. (a) Polarization curves for Pd@Pt/C MEA (Pt loading 0.04 mg cm^{-2}) and JM Pt/C MEA (Pt loading 0.1 mg cm^{-2}) as the cathode. The MEAs have identical anode Pt loadings (JM Pt/C 0.1 mg cm^{-2}). (b) Mass activities. The solid rectangle represents the mass activity in terms of metal, and the dashed rectangle represents the mass activity in terms of Pt.

impressive performance and achieved considerable output power density at 0.6 V. In particular, the mass-transport profile of the Pd@Pt/C MEA was improved significantly in the high current density area, indicating that the thinner catalyst layer shortened the proton pathway and promoted diffusion and transportation of the gases. Furthermore, the in situ electrochemical impedance results for the two MEAs (see Figure 8 and Table.1) were in good agreement with their single-cell performance, shown in Figure 7a. Only one semicircular loop can be observed in the Nyquist plot because the electrode process is dominated at low current densities by the ORR.[38] Apparently, the Pd@Pt/C MEA had the smaller charge transfer resistance, which suggested that the ultralow platinum loading MEA yielded a more efficient electrochemical active zone than did the conventional JM Pt/C MEA. As shown in Figure 7b, the mass activity (in terms of Pt mass) was also compared and presented a confirmative advantage of the Pd@Pt/C MEA. It can be seen that the Pt mass of the Pd@Pt/C MEA was 3.4 times higher than that of the JM Pt/C MEA, which demonstrated the superiority of the Pd@Pt/C MEA under the sluggish kinetics of the oxygen reduction reaction at the cathode.

Preliminary stability testing of the Pd@Pt/C as the cathode catalyst, presented in Figure 9, was conducted at 600 mA cm^{-2} for 150 h under constant discharge operation. It should be mentioned that no obvious decay in performance was observed for either the Pd@Pt/C MEA or the JM Pt/C MEA; actually, the Pd@Pt/C MEA suffered slight degradation in the beginning stage but stabilized after 20 h, indicating that its stability is comparable to that of JM Pt/C MEA.

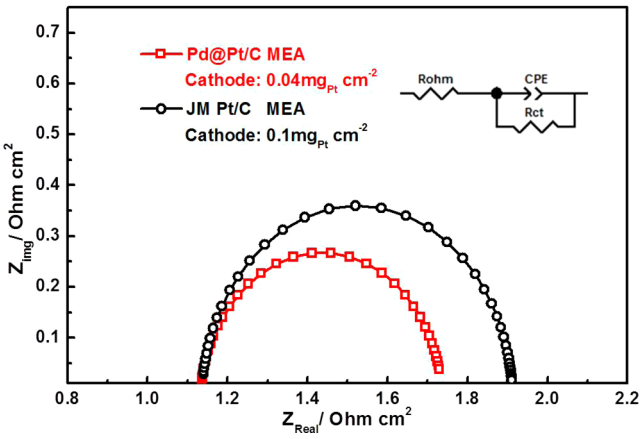

Figure 8. In situ electrochemical impedance curves of Pd@Pt/C MEA and JM Pt/C MEA at 0.8 V.

Table 1. Resistance of Single Cell with Two Types of MEAs

sample	Pd@Pt/C MEA	JM Pt/C MEA
R_Ω(Ω cm^2)	1.135	1.147
R_{ct}(Ω cm^2)	0.601	0.775

Regarding the greatly enhanced performance and excellent stability of our MEAs, we believe that they may be caused by following factors: (1) The very high dispersion of Pt. It was

DOI: 10.1021/acscatal.5b00030
ACS Catal. 2015, 5, 4318−4324

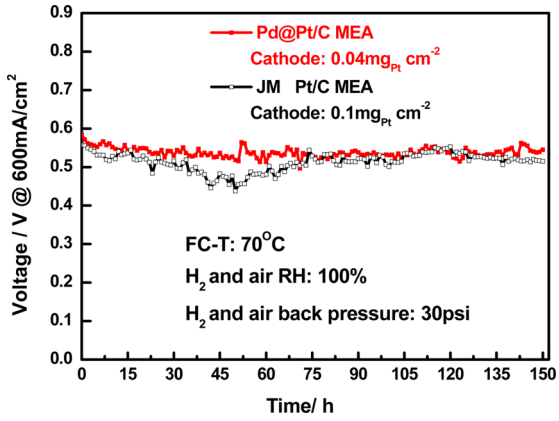

Figure 9. Preliminary stability test results for the Pd@Pt/C MEA and JM Pt/C MEA (600 mA cm^{-2} for 150 h).

confirmed by many researchers that the high dispersion of active components will result in high mass activity.[3,8] In our MEAs, the Pt atoms were deposited on the surface of Pd nanoparticles with a thickness of several atoms, therefore resulting in the greatly enhanced mass activity of Pt. (2) The high accessibility of the Pt. In our MEAs, almost all Pt atoms are accessible for the oxygen molecules because of the deposition pattern of the Pt atoms on the gas−liquid−solid interface (three-phase boundary), which is not covered by the binder or blocked by the support surface. (3) The interaction between the Pd in core and the Pt in shell layer improves the performance of the catalyst. It was reported by Adzic et al. and our group[12,39] that the increase in Pt mass activity is often much higher than the increase in the Pt exposure or Pt active surface area. A reasonable explanation for this phenomenon should be the interaction between the core and the shell. As demonstrated previously,[40,41] manipulating the surface electronic structure of Pt may have an impact on the ORR activity, resulting in more active Pt sites for the ORR. In this work, we found that our Pd@Pt/C MEA exhibits higher Pt^0 proportion revealed by XPS and lower charge transfer resistance than that of JM Pt/C MEA, confirming the performance improvement occurred by the interaction between the Pd core and the Pt shell. (4) The lattice strain caused by the deposition of Pt on the Pd core may also have contributed to the performance enhancement. It is suggested that the favorable lattice strain effects in changing the d-band center of the surface Pt atoms in the core−shell nanoparticles could contribute a lot to the enhancement in ORR activity.[41,42] It is well understood that the persistence of the OH groups on the Pt surface is a significant hindrance to ORR activity because of site blockage by OH.[43] Lowering the d-band center results in a decrease in the adsorption energy of the adsorbates to the Pt atoms, therefore accelerating the removal of OH and improving the ORR activity at last.[44,45] In this case, the lattice constants of Pt and Pd are 3.9232 and 3.8898 Å, respectively. When Pt atoms were deposited over the Pd core, the mismatch of the two elements would induce a lateral compressive strain of the surface Pt atoms relative to bulk Pt. The lattice constant calculated from the XRD pattern of Pd@Pt/C (Figure 3) is 3.8934 Å. The strain caused by the lattice compression would lead to a downward shift of the d-band center of Pt.[46] Accordingly, with a downward shift of the d-band centers, the Pd@Pt NPs can remove oxygenated species more easily than Pt/C NPs, resulting in enhanced ORR activity in this work. This is strongly supported by XPS observation, which has been reported and verified by other groups.[17,31,32] In addition, we believe the high stability of our Pd@Pt/C MEA should also be related to the strong interaction between the Pt in the shell layer and the Pd in the core.

4. CONCLUSION

Using a facile design process involving a PED approach, we fabricated a "green" MEA that has an ultralow Pt loading (0.015 mg cm^{-2} at the anode and 0.04 mg cm^{-2} at the cathode) with a novel Pd@Pt/C catalyst layer. Through in situ construction of active Pt nanoparticles directly on the surface of the Pd/C-base layer, the usage of platinum was significantly reduced. Furthermore, the novel Pd@Pt/C MEA exhibited enhanced performance as well as improved mass transfer in the single cell at both the anode and the cathode compared with JM Pt/C MEA, which may be owing to the catalyst layer's unique structure, high platinum dispersion, and interaction between the Pt shell and the Pd core. A more detailed study of this approach for fabricating the ultralow Pt loading MEA with improved ORR catalytic activity is forthcoming.

AUTHOR INFORMATION

Corresponding Author

*Fax: +86 20 87113586. E-mail: chsjliao@scut.edu.cn.

Notes

The authors declare no competing financial interest.

ACKNOWLEDGMENTS

We are grateful for financial support from the National Science Foundation of China (NSFC Project Nos. 21276098, 21476088, 51302091, U1301245), the Ministry of Science and Technology of China (Project No. 2012AA053402), the Guangdong Natural Science Foundation (Project No.S2012020011061), and the Department of Education of Guangdong Province (Project No. 2013CXZDA003).

REFERENCES

(1) Debe, M. K. *Nature* **2012**, *486*, 43−51.
(2) Winter, M.; Brodd, R. J. *Chem. Rev.* **2004**, *104*, 4245−4270.
(3) Gasteiger, H. A.; Kocha, S. S.; Sompalli, B.; Wagner, F. T. *Appl. Catal., B* **2005**, *56*, 9−35.
(4) Litster, S.; McLean, G. *J. Power Sources* **2004**, *130*, 61−76.
(5) Huang, S. Y.; Ganesan, P.; Popov, B. N. *ACS Catal.* **2012**, *2*, 825−831.
(6) Hwang, S. J.; Yoo, S. J.; Shin, J.; Cho, Y. H.; Jang, J. H.; Cho, E.; Sung, Y. E.; Nam, S. W.; Lim, T. H.; Lee, S. C.; Kim, S. K. *Sci. Rep.* **2013**, *3*, 1309.
(7) Hsieh, Y. C.; Zhang, Y.; Su, D.; Volkov, V.; Si, R.; Wu, L.; Zhu, Y.; An, W.; Liu, P.; He, P.; Ye, S.; Adzic, R. R.; Wang, J. X. *Nat. Commun.* **2013**, *4*, 2466.
(8) Dang, D.; Liao, S.; Luo, F.; Hou, S.; Song, H.; Huang, P. *J. Power Sources* **2014**, *260*, 27−33.
(9) Yin, A. X.; Min, X. Q.; Zhang, Y. W.; Yan, C. H. *J. Am. Chem. Soc.* **2011**, *133*, 3816−3819.
(10) Wang, L.; Nemoto, Y.; Yamauchi, Y. *J. Am. Chem. Soc.* **2011**, *133*, 9674−9677.
(11) Wang, D.; Xin, H. L.; Hovden, R.; Wang, H.; Yu, Y.; Muller, D. A.; DiSalvo, F. J.; Abruña, H. D. *Nat. Mater.* **2012**, *12*, 81−87.
(12) Yang, L.; Vukmirovic, M. B.; Su, D.; Sasaki, K.; Herron, J. A.; Mavrikakis, M.; Liao, S.; Adzic, R. R. *J. Phys. Chem. C* **2013**, *117*, 1748−1753.
(13) He, Q.; Shyam, B.; Nishijima, M.; Yang, X.; Koel, B.; Ernst, F.; Ramaker, D.; Mukerjee, S. *J. Phys. Chem. C* **2013**, *117*, 1457−1467.

DOI: 10.1021/acscatal.5b00030
ACS Catal. 2015, 5, 4318−4324

(14) Kulp, C.; Chen, X.; Puschhof, A.; Schwamborn, S.; Somsen, C.; Schuhmann, W.; Bron, M. *ChemPhysChem* **2010**, *11*, 2854−2861.
(15) Zhang, G.; Shao, Z. G.; Lu, W.; Xie, F.; Xiao, H.; Qin, X.; Yi, B. *Appl. Catal., B* **2013**, *132*−*133*, 183−194.
(16) Zhao, D.; Xu, B. Q. *Angew. Chem.* **2006**, *118*, 5077−5081.
(17) Alayoglu, S.; Nilekar, A.; Mavrikakis, M.; Eichhorn, B. *Nat. Mater.* **2008**, *7*, 333−338.
(18) Gao, H.; Liao, S.; Zeng, J.; Xie, Y. *J. Power Sources* **2011**, *196*, 54−61.
(19) Hartl, K.; Mayrhofer, K. J. J.; Lopez, M.; Goia, D.; Arenz, M. *Electrochem. Commun.* **2010**, *12*, 1487−1489.
(20) Zhang, W.; Wang, M.; Chen, J.; Romeo, T.; Harris, A. T.; Minett, A. I. *Electrochem. Commun.* **2013**, *34*, 73−76.
(21) Tian, Z. Q.; Lim, S. H.; Poh, C. K.; Tang, Z.; Xia, Z.; Luo, Z.; Shen, P. K.; Chua, D.; Feng, Y. P.; Shen, Z.; Lin, J. *Adv. Energy. Mater.* **2011**, *1*, 1205−1214.
(22) Wee, J.-H.; Lee, K.-Y.; Kim, S. H. *J. Power Sources* **2007**, *165*, 667−677.
(23) Rabis, A.; Rodriguez, P.; Schmidt, T. J. *ACS Catal.* **2012**, *2*, 864−890.
(24) Su, H. N.; Liao, S. J.; Shu, T.; Gao, H. L. *J. Power Sources* **2010**, *195*, 756−761.
(25) Liao, S.; Holmes, K. A.; Tsaprailis, H.; Birss, V. *J. Am. Chem. Soc.* **2006**, *128*, 3504−3505.
(26) Skriver, N. M. R. H. L.; Rosengaard, N. M. *Phys. Rev. B: Condens. Matter Mater. Phys.* **1992**, *46*, 7157−7168.
(27) Yang, J.; Cheng, C. H.; Zhou, W.; Lee, J. Y.; Liu, Z. *Fuel Cells* **2010**, *10*, 907−913.
(28) Nishanth, K. G.; Sridhar, P.; Pitchumani, S. *Int. J. Hydrogen Energy* **2013**, *38*, 612−619.
(29) Nilekar, A. U.; Xu, Y.; Zhang, J.; Vukmirovic, M. B.; Sasaki, K.; Adzic, R. R.; Mavrikakis, M. *Top. Catal.* **2007**, *46*, 276−284.
(30) Lewera, A.; Zhou, W. P.; Hunger, R.; Jaegermann, W.; Wieckowski, A.; Yockel, S.; Bagus, P. S. *Chem. Phys. Lett.* **2007**, *447*, 39−43.
(31) Richter, B.; Kuhlenbeck, H.; Freund, H. J.; Bagus, P. S. *Phys. Rev. Lett.* **2004**, *93*, 026805(1)−026805(4).
(32) Yang, J.; Zhou, W.; Cheng, C. H.; Lee, J. Y.; Liu, Z. *ACS Appl. Mater. Interfaces* **2010**, *2*, 119−126.
(33) Karlberg, G. S. *Phys. Rev. B: Condens. Matter Mater. Phys.* **2006**, *74*, 153414.
(34) Stamenkovic, V. R.; Mun, B. S.; Mayrhofer, K. J. J.; Ross, P. N.; Markovic, N. M. *J. Am. Chem. Soc.* **2006**, *128*, 8813−8819.
(35) Hammer, B.; Nørskov, J. K. *Adv. Catal.* **2000**, *45*, 71.
(36) Shao, M.; Sasaki, K.; Marinkovic, N.; Zhang, L.; Adzic, R. *Electrochem. Commun.* **2007**, *9*, 2848−2853.
(37) Sasaki, K.; Naohara, H.; Cai, Y.; Choi, Y. M.; Liu, P.; Vukmirovic, M. B.; Wang, J. X.; Adzic, R. R. *Angew. Chem., Int. Ed.* **2010**, *49*, 8602−8607.
(38) Yuan, X.; Wang, H.; Colinsun, J.; Zhang, J. *Int. J. Hydrogen Energy* **2007**, *32*, 4365−4380.
(39) Adzic, R. R.; Zhang, J.; Sasaki, K.; Vukmirovic, M. B.; Shao, M.; Wang, J. X.; Nilekar, A. U.; Mavrikakis, M.; Valerio, J. A.; Uribe, F. *Top. Catal.* **2007**, *46*, 249−262.
(40) Zhang, J.; Mo, Y.; Vukmirovic, M. B.; Klie, R.; Sasaki, K.; Adzic, R. R. *J. Phys. Chem. B* **2004**, *108*, 10955−10964.
(41) Greeley, J.; Norskov, J. K.; Mavrikakis, M. *Annu. Rev. Phys. Chem.* **2002**, *53*, 319−348.
(42) Kibler, L. A.; El-Aziz, A. M.; Hoyer, R.; Kolb, D. M. *Angew. Chem., Int. Ed.* **2005**, *44*, 2080−2084.
(43) Wang, J. X.; Markovic, N. M.; Adzic, R. R. *J. Phys. Chem. B* **2004**, *108*, 4127−4133.
(44) Markovic, N. M.; Ross, P. N. *Surf. Sci. Rep.* **2002**, *45*, 117−229.
(45) Mavrikakis, M.; Hammer, B.; Norskov, J. K. *Phys. Rev. Lett.* **1998**, *81*, 2819−2822.
(46) Kitchin, J. R.; Nørskov, J. K.; Barteau, M. A.; Chen, J. G. *J. Chem. Phys.* **2004**, *120*, 10240−10246.

DOI: 10.1021/acscatal.5b00030
ACS Catal. 2015, 5, 4318−4324